Fuel 289 (2021) 119922

Contents lists available at ScienceDirect

Fuel

journal homepage: www.elsevier.com/locate/fuel

Full Length Article

Finite rate simulations and analyses of wet/distributed flame structure in swirl-stabilized combustion

Kai Zhang *, Yazhou Shen, Christophe Duwig

Department of Chemical Engineering, Royal Institute of Technology (KTH), Brinellvägen 8, 114 28 Stockholm, Sweden

ARTICLE INFO

Keywords:
Humidified gas turbine
Colorless distributed combustion
CEMA
Wet/steam diluted combustion
Flame regime transition

ABSTRACT

Towards developing humidified gas turbines (HGT) capable of running at high electrical efficiencies and low emissions, wet/steam-diluted combustion in a premixed swirl burner is investigated using large eddy simulation and a partially stirred reactor method. Chemical explosive mode and extended combustion mode analyses are performed to promote the understanding of wet flame structures. The former identifies the key features of the wet methane oxidation processes, and the latter extends the flame regime classification method to describing the combustion status of fluid parcels using local properties. Three combustion regimes are extensively discussed: the swirl stabilized (SS), colorless distributed (CDC) and non-combustible. Using the combined analyses of the two approaches, it is found that compared to dry flames, wet flames present more fluid parcels defined in the practical CDC regime where local heat release is low and Damköhler number is smaller than unity. The wet fluid parcels are capable of self-igniting via radical explosion, while dry fluid parcels self-ignite via thermal runaway. The species CH_2O and temperature are the first and second highest contributors towards the explosivity of dry flames, while temperature is insignificant to that of wet flames. The species C_2H_6 is found an important source to the self-ignitability of wet fluid parcels in the practical CDC regime due to the activation of the three-body ethane formation reaction R148: $2CH_3 + M = C_2H_6 + M$ in the low O_2% wet combustion environment. Proper use of proposed methods to quantify wet flame behavior guides stable and low emission operation of practical HGT.

1. Introduction

In response to climate change and the depletion of fossil fuels, the European commission targets to cut down greenhouse gas emissions by at least 40% below the 1990 level and to improve energy efficiency by 32.5%, by 2030 [1]. Also, in line with the United Nation Sustainable Development goal #7 – clean and affordable energy, industry will be decarbonized. It implies a significant increase in renewable electricity (solar, wind, biomass, geothermal, *etc*) and novel solutions to balance the fluctuating production and demand. For the last challenge, the humidified gas turbine (HGT) cycle is an attractive solution [2,3] due to its rapid response to the demand and high electrical efficiency. There are several variations of HGT such as water or steam injected gas turbines, evaporative gas turbines (EvGT) or humid air turbines (HAT), *etc*. [4,5]. At the heart of these technologies, the wet combustion technology (high steam-dilution of fuel) is known capable of reducing NO_x emissions and improving electrical efficiencies, compared to dry operation. The former is realized by controlling wet flame temperature, eliminating flame fronts, and overcoming sharp temperature gradients [6–8]. The latter is achieved by reducing the power consumption of the air compressor since the direct-injected high-temperature steam replaces part of the airflow. Burning high steam-diluted fuels in the combustor leads to wet flames that fall in the distributed combustion regime and could be referred to as flameless combustion (FC) or colorless distributed combustion (CDC) regime. The former terminology is often used in Germany, and the latter in the United States [9]. These regimes denote a distributed reaction zone as opposed to the thin reaction zones in conventional flames [10]. The spectacular feature is that only weak emission of visible radiation can be detected during the combustion process [11]. Also, these regimes have similarities to the MILD (Moderate or Intense Low oxygen Dilution) regime [12] – although the oxygen concentration is not necessarily low and preheating does not reach the 1000 °C level.

Despite the known advantages of using wet combustion in the HGT cycle, combustors capable of running on high steam-diluted fuels are still few. It follows the youth of this concept and is due to an insufficient understanding of the flow and flame structures in the CDC regime. A small perturbation in the fuel composition may easily lead to flame blow-off at the aforementioned working conditions [13,14]. Hence, a key feature for sustainable operation in the FC or CDC regime lies in the

* Corresponding author.
E-mail addresses: kaizhang@kth.se (K. Zhang), yashen@kth.se (Y. Shen), duwig@kth.se (C. Duwig).

https://doi.org/10.1016/j.fuel.2020.119922
Received 31 August 2020; Received in revised form 7 November 2020; Accepted 29 November 2020
Available online 16 December 2020

Nomenclature

Da	Damköhler number
Da_{IG}	Ignition Damköhler number
D_{cb}, D_{mix}	Combustor, mixing tube diameter (m)
Ka	Karlovitz number
$L_{cb,\ exp}$	Experimental combustor length (m)
P_{th}	Thermal power (W)
Re	Reynolds number
S	Swirl number
S_L	Flame speed (m/s)
t_{res}	Flow residence time (s)
T_w, T_{ad}	Wall, adiabatic flame temperature (K)
T_{in}, T_{max}	Mixture inlet, maximum temperature (K)
T_c, T_{ign}	Cell center, self-ignition temperature (K)
U_0	Bulk velocity (m/s)
$U_z^{'}$	Velocity fluctuation in axial direction (m/s)

Greek symbols

τ_{mix}, τ_c	Mixing, chemical time scale (s)
τ_{ig}	Ignition time (s)
Ω	Mass-based steam to air ratio
δ_L	Thermal flame thickness (m)
ϕ	Equivalence ratio
ρ	Density (Kg/m^3)
κ	Segregation factor
Δ	Grid size (m)
Δ_t	Physical time step (s)
λ_ω	Eigen value

combustion stabilization [15]. Fuel and hot burnt products are extensively mixed and burnt in a very short residence time, typically $1 \sim 3\ ms$ [8]. Strong swirling flow aids the achievement of the extensive mixing, and fuel dilution ensures that a mixing time scale τ_{mix} is much smaller than chemical time scale τ_c – an essential criterion for CDC where the Damköhler number $Da = \tau_{mix}/\tau_c < 1$. In relation to this, one other complementary criterion is that local fluid parcels can be ignited by rapid mixing with high temperature burnt product rather than by high heat release locally. Consequently, a practical CDC flame is characterized by the locally low heat release rate – hence the flame is colorless. Based on these definitions, the achievement of FC or CDC flame is not limited by the inclusion of recirculating steam in HGT. Any kind of hot product recirculation can lead to similar flame behavior.

Among pioneering studies, CDC has been investigated both experimentally [8,16–20], and numerically [6,10,21,22]. Khalil and Gupta [17–19] conducted a series of experimental studies in a non-premixed swirl burner. Methane combustion in the N_2/CO_2 diluted air showed significantly low NO emission compared to that in the pure air environment. An oxygen reduction by 3% in the air-path reduced NO by nearly 60% with little impacts on the CO emission [17]. An observation of the de-coupled signal between OH-PLIF and velocity fluctuation was reported implying a more stable reaction zone (lower fluctuation level) for CDC than conventionally undiluted flames [18]. A recent work by Roy and Gupta [20] documented experimental observations of the flame shapes, flame expansions, and emission characteristics of burning different fuels (CH_4, H_2-CH_4, and C_3H_8) in the same burner and with the same dilutants. Compared to N_2 diluted flames, CO_2 diluted flames showed higher lift-off height due to the larger heat capacity of this dilutant. At an intermediate level of O_2 ($18 \sim 19\%$vol. in the oxidizer path), CO_2 dilution increased CO emission due to the promoted high-temperature CO_2 dissociation reaction: $CH_2(s) + CO_2 = CO + CH_2O$.

Numerical studies present some in-depth physicochemical behaviors of FC, CDC, or mild combustion. Duwig et al. [10] studied a propane-air fuelled flameless burner featuring 12 equally spaced injectors. Turbulent coherent structures and fuel oxidation processes were investigated using Large Eddy Simulation (LES) with a look-up table built for detailed chemistry. FC mode occurred when fresh gases are diluted with the same amount of vitiated gases before combustion. Later, Fooladgar et al. [6] investigated flameless combustion using the LES-PaSR model with a finite rate chemistry method (38 species and 173 reactions). The transition of flame from the conventional thin reaction regime to the FC regime was reported for the same burner. Krüger et al. [22] investigated dry and wet methane combustion in a premixed swirl burner using LES and thickened flame model (TFM). Proper orthogonal decomposition (POD) analysis showed differences in the coherent structure dynamics while moving from conventional to wet combustion. Pressure impact (up to 8 atm) on MILD combustion was extensively investigated by Tu et al. [23] in a methane fuelled bluff-body burner. High pressure switched combustion from MILD to conventional regime due to the weakened mixing strength. This can be compensated via reducing air nozzle diameter which strengthened internal flue gas recirculation. In addition, they reported that high pressure can activate strong fuel decomposition reactions and cause a larger difference between positive and negative heat release rate – in contrast to MILD combustion featuring more homogeneous heat production. Chemical kinetic modeling using a counterflow flame configuration showed that low oxygen concentration is a key to MILD combustion irrespective of pressure. A study by Mardani et al. [24] showed that the higher hydrocarbon oxidation pathway has a significant contribution to CO formation under mild combustion of methane/air mixtures.

Although these studies have provided valuable knowledge about the FC, CDC, or mild combustion, no attempts have been made yet to understand the impact of high steam dilution on the CDC flame structures in a premixed swirl burner. The lack of this knowledge partly limits the commercial demonstration of wet combustion technology in advanced power cycles. To that end, Chemical Explosive Mode Analysis (CEMA) technique is used in the present work to explore more details in a more complex flow environment. The method provides unique insights into the flame structure, stability, ignition, *etc.* by performing a chemical Jacobian matrix analysis. Wang et al. [25] employed CEMA and reported the importance of temperature domination to the pre-heating of 1D laminar H_2-air premixed flame. In a perfectly stirred reactor, two ignition stages of hydrogen-air combustion were reported: the radical explosion and thermal runaway stages – an observation also mentioned by Lu et al. [26]. Cifuentes et al. [27] numerically investigated a CH_4-H_2-air fuelled, Jet-in-Hot-Coflow burner. Lean and rich flame fronts in the MILD combustion regime were detected by CEMA. Excess O_2% in the hot oxidant stream promoted the probability of finding explosive fluid parcels in the central jet. To the best of the author's knowledge, previous studies using CEMA have only focused on non-steam diluted, simple jet flames [25–29].

The present work is the first attempt to provide a new understanding of the steam dilution effect on the kinetics of wet combustion in a swirl burner. High fidelity large-eddy simulations of a premixed swirl burner are performed. Different steam-to-air ratios are explored at a constant thermal power of 63 kW. For enabling CEMA, a detailed, finite rate chemistry method is used. For the first time, two other extended combustion mode analyses are performed to assist the CEMA analysis of wet combustion. A detailed flame regime classification graph is proposed to illustrate the concepts behind the choices. The present paper is structured as follows. Section 2 summarizes the methods employed and introduces the experimental and numerical setups. Section 3 discusses the impact of steam on the flow and flame structures of wet methane combustion. Finally, conclusions of the present work are given in Section 4

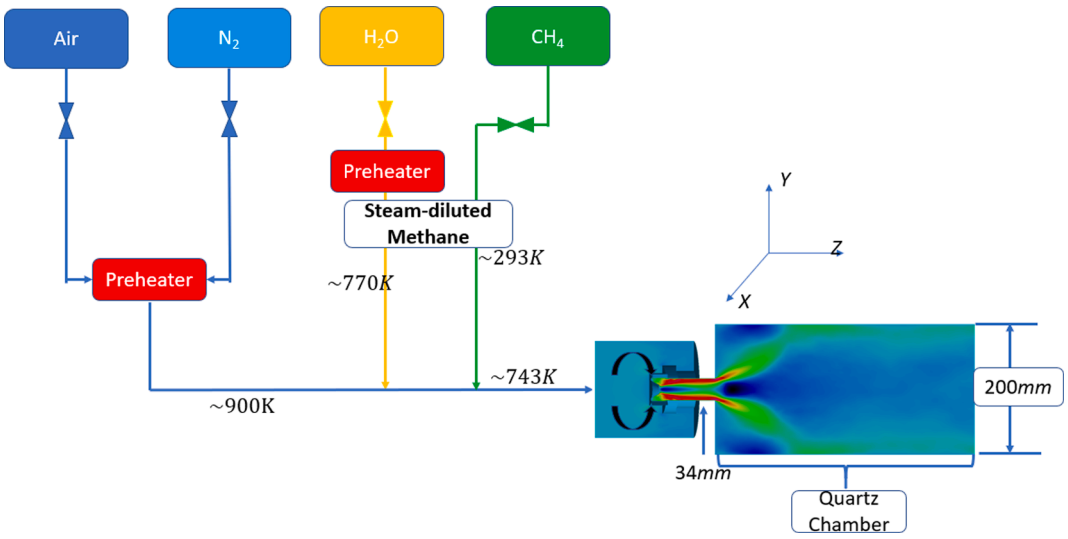

Fig. 1. Sketch of the experimental rigs and detailed operating configurations.

Table 1
Experimental and numerical conditions.

	Ω(%)	ϕ	T_{in} (K)	CH_4 (Kg/h)	H_2O (Kg/h)	O_2 (mol%)	U_0 (m/s)	S_L (m/s)	δ_L (m)	*Re*	*Ka*
NGL0	0	0.61	293	4.6	0	19.7	34.7	1.20	3.9×10^{-4}	76,900	1
NGH0	0	0.42	743	4.6	0	20.1	126.4	0.52	6.7×10^{-4}	57,400	30
NGH1	20	0.60	743	4.6	27	15.1	117.7	0.38	9.4×10^{-4}	51,100	50
NGH2	30	0.68	743	4.6	34	13.6	115.4	0.33	1.1×10^{-3}	49,500	60

with novel findings highlighted.

2. Presentations of the investigations

2.1. The wet-combustion burner experiment at TU Berlin

The setup corresponding to a 63 kW swirl burner operated at TU Berlin is shown in Fig. 1. It was designed to enable experimental and numerical studies for understanding the flow and flame structures in wet combustion, and to offer optical access. This burner can be fuelled with different air premixed mixtures at an atmospheric pressure including the steam-diluted methane (CH_4/H_2O) and steam-diluted bio-syngas fuels ($CO/CO_2/H_2/CH_4/H_2O$) as thoroughly discussed by Dybe et al. [30]. In the present study, we focus on diluted methane flames. During the experiment, the air and N_2 streams are preheated to ~ 900 K, the steam is preheated to ~ 770 K, and the methane is supplied at ~ 293 K. The resulting fuel/air/steam mixtures are injected at ~ 743 K and enter the burner through a radial swirler with a geometric swirl no. estimated to be $S = 0.9$ [31]. A quartz made, transparent combustion chamber of diameter $D_{cb} = 0.2$ m and length $L_{cb,\,exp} = 0.3$ m enables optical access to the flame location. It is then followed by a long steel made exhaust tube of the same diameter. The high swirl creates a central recirculation zone (CRZs) and outer recirculation zone (ORZs) with a flame stabilized in between [32]. The flame shapes and positions are captured by OH* chemiluminescence using an intensified CCD camera with band-pass filtering between 295 and 340 nm. A total of 480 images are taken for each test at a frequency of 5 Hz and are used for averaging. Two K-type thermocouples are used to measure quartz chamber outer wall temperature T_w at 0.41 m and 0.99 m downstream the exit of the mixing tube ($D_{mix} = 0.034$ m). This temperature varies between 750 K and 850 K for different cases. Considering the low thermal conductivity of quartz glass and the lack of metal combustor for accurate wall temperature measurement, a constant temperature $T_w = 1000$ K will be chosen for the numerical simulations in the present work. More details of the employed burner can be found in previous studies [33,34].

The experimental and numerical conditions for the wet methane combustion are summarized in Table 1. Four cases are simulated while only the two wet flame cases: the NGH1 and NGH2 are experimentally studied. More experimental observations at various combustion conditions can be found in [35]. The nomenclature is defined as follows: NGH0, NGH1, and NGH2 denote combustion with high inlet temperature ($T_{in} = 743$ K). The 'NG' stands for 'natural gas' and 'H' stands for 'High' inlet temperature. The NGL0 is a particular case simulated to observe the effect of inlet temperature, hence the mixtures are non-preheated and non-diluted with $T_{in} = 293$ K. The '0' can be used as an indicator of dry combustion which also applies to the case NGH0 with the steam-to-air ratio $\Omega = \dot{m}_{H2O}/\dot{m}_{air} = 0\%$. Using mass-based Ω follows the convention of industrial applications. In Table 1, the U_0, S_L, and δ_L are the bulk velocity at the exit of the mixing tube, the laminar flame speed, and the flame thermal thickness respectively. From NGH0 to NGH2, the increase of Ω and decrease of O_2% enable flame regime transition from the conventional to the FC. A global Karlovitz number *Ka* is defined as $Ka\ (U_z'/S_L)^{1.5}(\delta_L/D_{mix})^{0.5}$. The instantaneous fluctuation along the shear layer of the annular jets can be intermittently up to ~ 10 times larger than U_z' at the exit of the mixing tube, leading to locally much higher *Ka* than the one estimated presently. The δ_L is obtained from the thermal thickness of premixed laminar flames, while it is locally perturbed by turbulence and thickened significantly by dilution with vitiated burnt gases, intermittently leading to 10 ~ 100 times larger *Ka* locally, as reported by Duwig et al. [36]. Accordingly, all wet methane flames investigated are essentially high *Ka* flames with local $Ka > 100$ [37,38].

In the present work, two important factors are kept constant for the convenience of investigating the flow and flame structures of wet/CDC combustion: the adiabatic flame temperature T_{ad} and the thermal power P_{th}. The former is calculated using the Cantera package [39] and is kept

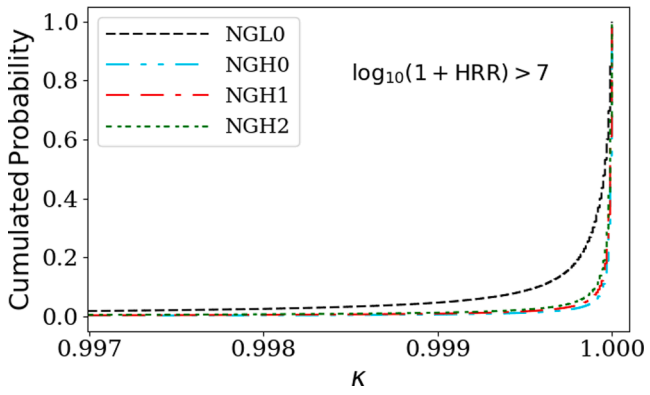

Fig. 2. Cumulative probability distribution of κ.

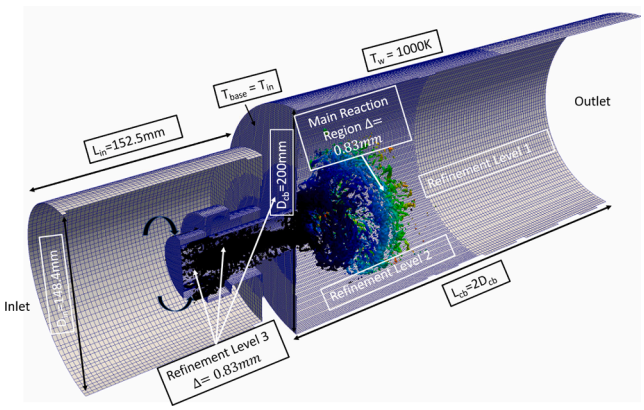

Fig. 3. Numerical setup of the burner with vortices obtained using Q-criterion.

at ~ 1690 K by co-varying the steam-to-air ratio Ω and the fuel–air equivalence ratio ϕ, written as {Ω, ϕ}; and the latter is set at $P_{th} = \dot{m}_{CH4} \times LHV_{CH4} \approx 63KW$. There are two reasons to keep the flame temperature constant: first, combustion instability is influenced by the ratio T_{ad}/T_{in} [40,41] and we choose to focus on the stable cases; and second, NO_x emission can be minimized via inhibiting its chemical pathway below 1700 K. The temperature jump across the NGH flames is $T_{max}/T_{in} \sim 2.3$ with $T_{in} = 743$ K, and $T_{max}/T_{in} \sim 5$ for the NGL0 case with $T_{in} = 293$ K, as will be reported in Section 3.2. The T_{max} is the local maximum temperature from LES prediction and is lower than T_{ad}. The constant power and flame temperature assumptions enable us to compare the effect of dilution by steam alone.

2.2. Solver, equations, and closures

The swirl burner shown in Fig. 1 is numerically simulated using an in-house variant of reactingFoam solver enforcing a low-Mach (LM) number assumption [22,42,43]. Under the assumption, the mixture density is decoupled from the thermodynamic pressure and is dependent on a reference pressure p_0, written as $\overline{\rho} = \overline{(p_0/RT)}$. The solver essentially solves equations for four LES filtered variables: mass, momentum, species, and enthalpy [10,44]. Introducing Favre-averaging to the momentum equation leads to an unresolved term modeled as,

$$\tau_{ij} = \widetilde{u_i u_j} - \tilde{u}_i \tilde{u}_j = \frac{2}{3} k_{sgs} \delta_{ij} - 2\nu_{sgs} \tilde{S}_{D_{ij}} \tag{1}$$

Where the sub-grid scale (SGS) kinetic energy k_{sgs} is obtained using the wall adaptive local eddy viscosity (WALE) method [45,46].

To close species equations, the filtered species reaction rate is evaluated with a PaSR model [47], using a factor κ to segregate the reacting and non-reacting fractions of cells:

$$\overline{\dot{w}_j(Y_i, T)} = \kappa \dot{w}_j(\tilde{Y}_i, \tilde{T}) \tag{2}$$

Where the $\dot{w}_j(\tilde{Y}_i, \tilde{T})$ is the rate of formation of species Y_i, calculated from Arrhenius expression. In the present work, a skeletal mechanism (hereafter called SK30) for methane combustion is used [48]. It contains 30 species and 184 reactions and has been derived from the GRI-Mech 3.0. The same modeling choice was made by Cifuentes et al. [27] and was shown to provide an accurate description of the distributed combustion including detailed oxidation chemistry.

The present tool is supplemented by 14 reactions for capturing OH* of Kathrotia [49]. The accuracy of the SK30 is validated by comparing the predicted flame speed against experimental measurements in a high steam-diluted combustion environment, as given in Appendix B. A comparison of flame shapes predicted using the Kathrotia OH* mechanism and that proposed by Hall and Petersen [50] was also performed, while little differences are observed and are hence not reported here.

The segregation factor κ used in equation (2) is traditionally modeled as [51],

$$\kappa = \frac{\tau_c}{\tau_c + \tau_{mix}} \tag{3}$$

We tested the influence of the model and observed that κ remains close to unity in the present results. Fig. 2 shows how cumulated probability varies with respect to κ sampled in the main flame region featuring high log-based heat release rate (HRR): $log_{10}(1 + HRR) > 7$ (conditioning to regions of significant heat-release). A rapid increase of probability is observed only until near-unity κ, indicating a very low probability (frequency) of finding small κ. Therefore, all flames investigated in the present work are characterized by longer chemical reaction time than mixing time and that the contribution of the subgrid-scale model is marginal. It validates the choice of the present model.

2.3. Numerical setups

The numerical setup of the burner is shown in Fig. 3. A hexahedral dominant mesh, which contains 3.7 million cells, is obtained with SnappyHexMesh utility in OpenFOAM v5 [52]. Grid independence studies are performed and reported in Appendix A. It is shown that increasing further the cell size does not modify the result. For the present work, the combustion chamber of $D_{cb} = 0.2\,m$ is used, and the grid resolution in the mixing tube, swirler, and the main reaction region is $\Delta = 8.3 \times 10^{-4} m$. This yields 41 cells over the diameter of the mixing tube. The resolution is comparable to those reported in the literature [42,43] and is smaller than the wet flame thermal thickness. The distribution of cell size is shown in Fig. 3 with the smaller cells in the region of vortex breakdown and flame stabilization. The length of the combustor simulated is $L_{cb} = 2D_{cb} = 0.4$ m.

At the inlet of the burner, a zero gradient Neumann boundary condition is imposed on the pressure, while a Dirichlet boundary condition is applied to other variables such as velocity, species mass fraction, *etc.* At the outlet, the Neumann boundary condition is applied to all variables. The combustor wall is set with $T_w = 1000$ K and a non-slip condition is employed. The base of the combustion chamber is forced with a lower temperature $T_{base} = T_{in}$, the inlet temperature of the mixtures. All conservation equations are discretized using the 2nd order spatial (linear flux reconstruction) and temporal schemes [53,54]. An implicit PISO algorithm with four corrector steps is used for time integration. The maximum Courant-Friedrich-Levy number is set at 0.5. The physical time-steps $\Delta_t \approx 1 \times 10^{-6} s$ for the low T_{in} case and $5 \times 10^{-7} s$ for the high T_{in} cases are automatically adjusted based on the maximum allowed Courant number. In the main flame region, the typical Courant number is below 0.2. Due to different bulk velocities of the low and high T_{in} cases, the flow residence time for the former is $t_{res} = L_{cb}/U_0 \approx 10ms$ and

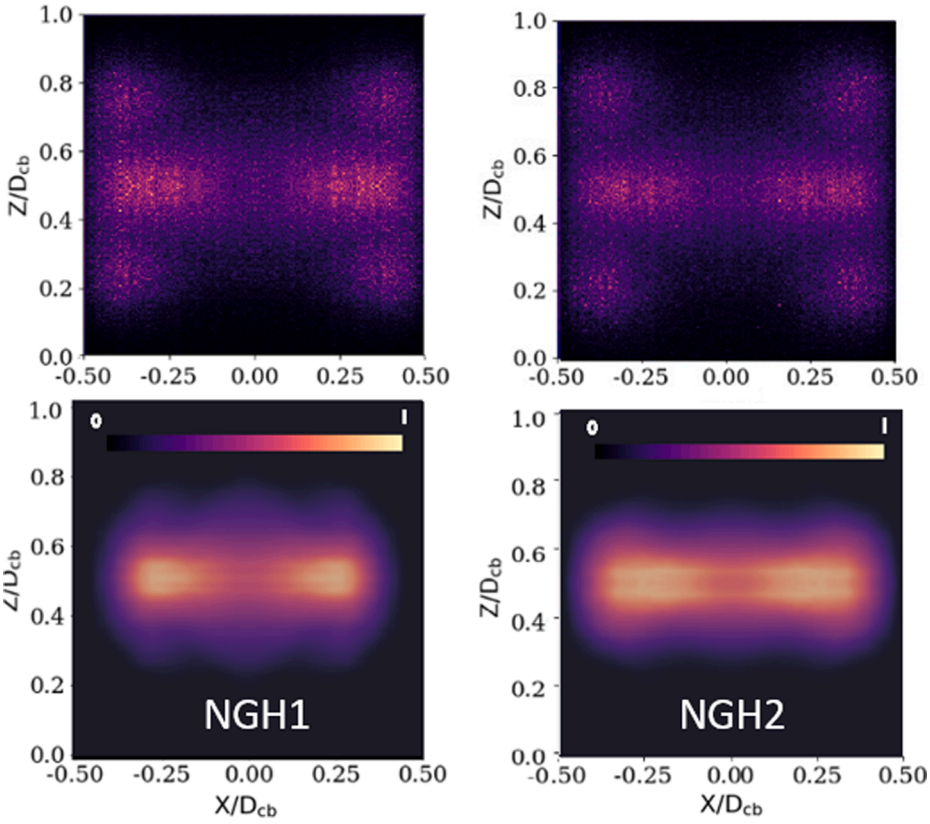

Fig. 4. Chemiluminescent OH* comparison between numerical prediction (bottom) and experimental observation (top). Images are normalized by local OH* intensity maxima.

the latter is 4*ms*. During the running of these cases, the low T_{in} case is first run for 0.14 *s*, then averaged until 0.42 *s* physical time. The high T_{in} cases are run for half of the time. Consequently, all cases are averaged over roughly 30 flow-through times.

2.4. Chemical explosive mode analysis (CEMA)

For analyzing the structure of the reaction layer and understanding the different reactions at play, CEMA is employed. In particular, it is used to detect the pre- and post-ignition zones of methane combustion in a swirl burner, and to identify the key features of the methane oxidation processes as a function of the dilution by steam. CEMA was developed by Lu et al. [26] as a post-processing diagnostic tool to identify flame stabilization mechanisms in the lifted jet flames. Applying this method to the present cases is relevant as the reaction zone detaches from the burner base and often presents features similar to the lifted flames. The theoretical base of CEMA is described in the literature [25–28], only a brief description of this method is provided below.

For a typical reacting flow, governing equations for species and temperature can be generalized as:

$$\frac{D\boldsymbol{y}}{Dt} = \omega(\boldsymbol{y}) + s(\boldsymbol{y}) \tag{4}$$

Where D/Dt represents the material derivative and $\boldsymbol{y} = [Y_1, Y_2 \cdots Y_n, T]$ is the thermo-chemical state vector. The $\omega()$ is the chemical source term and the non-chemical terms such as mixing and diffusion are gathered in $s()$.

The chemical Jacobian $\boldsymbol{J}_{\omega_{ij}}$, composed of the derivatives of the chemical reaction rate can be written as:

$$\boldsymbol{J}_{\omega_{ij}} = \frac{d\omega_i}{dy_j} = \begin{bmatrix} \frac{\partial\omega_1}{\partial y_1} & \cdots & \frac{\partial\omega_1}{\partial y_n} \\ \vdots & \ddots & \vdots \\ \frac{\partial\omega_n}{\partial y_1} & \cdots & \frac{\partial\omega_n}{\partial y_n} \end{bmatrix} \tag{5}$$

The Jacobian matrix is diagonalized giving the matrix $\boldsymbol{\Lambda}$ with the eigenvalues λ_{ii} and two eigenvector matrices $\boldsymbol{A}_{\omega_{ij}}$ (right), $\boldsymbol{B}_{\omega_{ij}}$ (left), written as:

$$\boldsymbol{\Lambda} = \boldsymbol{B}_{\omega_{ij}} \boldsymbol{J}_{\omega_{ij}} \boldsymbol{A}_{\omega_{ij}} \tag{6}$$

A complex eigenvalue of $\boldsymbol{J}_{\omega_{ij}}$ indicates the existence of the chemical explosive mode (CEM) in an oscillatory type, with the maximum real part of λ_{ii}, denoted as $Re(\lambda_\omega)$ corresponding to the reciprocal time scale of the chemical reaction time τ_c and the imaginary part corresponding to the oscillation frequency [26].

The CEMA inherits the concept of the mode of computational singular perturbation (CSP) [55,56], but differs from it as the latter involves the decomposition of not only the $\omega(\boldsymbol{y})$ but also the mixing/diffusion term $s(\boldsymbol{y})$ in equation (4). Hence, the explosive mode indicates the degree of the propensity of isolated mixtures towards ignition, whilst only considering their chemical reactivities. For instance, mixtures are explosive if $Re(\lambda_\omega) > 0$ and non-explosive if $Re(\lambda_\omega) < 0$, each representing unburnt and burnt mixtures. The high CEM of mixtures is the fastest decaying mode determining the rate at which the status of mixtures is pushed to equilibrium. The interface between the burnt and the unburnt mixtures is hence the ignition boundary, formed by points crossing $Re(\lambda_\omega) = 0$. In the present work, the visualization of λ_ω follows the expression in [27,28] and is written as,

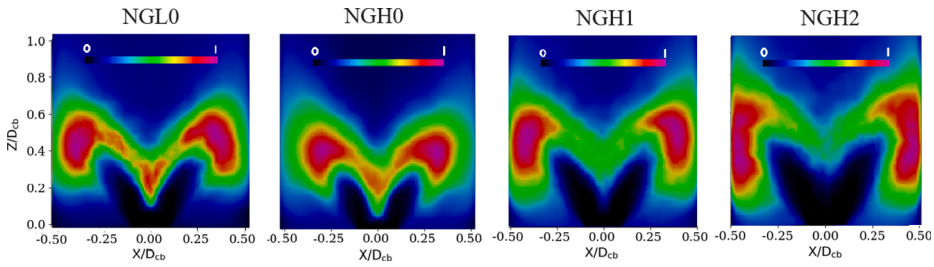

Fig. 5. Simulated time-averaged OH distribution. Images are normalized by image OH maximum.

$$Re(\lambda_\omega) = sign(Re(\lambda_\omega)) \times log_{10}(1 + |Re(\lambda_\omega)|) \tag{7}$$

Where *sign*() is the signum function. In the PaSR modeling approach, a computational cell is divided into two fractions: a reacting and a non-reacting fraction by a separation factor κ, defined in equation (3). To perform CEMA in association with the PaSR modeling approach, the first term on the right-hand side of the equation (4) should be written as $\kappa \times \omega(\boldsymbol{y})$. In the present work, owing to the high *Ka* nature of the flames in the CDC regime with $\tau_{mix} \ll \tau_c$, the original chemical Jacobian is still retained as $\kappa \approx 1$.

Following the CSP concept, the species and reactions contributing to CEMs can be tracked invoking the explosion index (EI) and the participation index (PI) [26,56] giving,

$$EI = \frac{\left|\boldsymbol{A}_{\omega_{i,j}} {}^{\circ} \boldsymbol{B}^{\boldsymbol{T}}_{\omega_{i,j}}\right|}{sum\left(\left|\boldsymbol{A}_{\omega_{i,j}} {}^{\circ} \boldsymbol{B}^{\boldsymbol{T}}_{\omega_{i,j}}\right|\right)}, \qquad PI = \frac{\left|\left(\boldsymbol{B}_{\omega_{i,j}} \cdot \boldsymbol{\upsilon}\right)^{\circ} \Re\right|}{sum\left(\left|\left(\boldsymbol{B}_{\omega_{i,j}} \cdot \boldsymbol{\upsilon}\right)^{\circ} \Re\right|\right)} \tag{8}$$

Where the $\cdot$ and $^{\circ}$ represent the dot and the elementary-wise multiplication respectively. The $\boldsymbol{\upsilon}$ and $\Re$ are the stoichiometric coefficients of species and the volume-specific stoichiometric reaction rates for each reaction. Note that the matrix $\boldsymbol{\upsilon}$ contains an extra row denoting the change in enthalpy for each reaction [25]. Both EI and PI are normalized vectors ranging from zero to unity. The large EI and PI values denote the leading role of typical species (or temperature) and participation reactions to CEMs. For swirl stabilized flames, the dominating role of species contribution (Υ_{EI}) to CEMs of $Re(\lambda_\omega) > 0$ may be viewed as a sign for self-ignition in the CDC regime, while the temperature (T_{EI}) contribution implies a feature of conventional flames.

3. Results

3.1. Comparison with experimental data

In Fig. 4, the predicted OH* intensities of the cases NGH1 and NGH2 are qualitatively compared with experimental observations. The top images are obtained from averaging 480 experimental snapshots. The bottom images are Abel transformed (line of sight integration) results of the time-averaged OH* prediction. Chemiluminescent OH* (excited hydroxyl radical) can often be used as an indicator of heat release boundary or peak heat release, primarily produced via the CH reaction: $CH + O_2 = CO + OH^*$. A central lifted flame sitting in between $Z/D_{cb} \approx 0.4$ and 0.6 is observed in both experimental and numerical results. Increasing Ω from 20% to 30% has little impact on the flame shape that the NGH1 flame is only slightly longer in axial *Z* and shorter in spanwise *X* directions compared to NGH2. The OH* intensity in the top images differs from that in the bottom due to an observation of four low OH* intensity, circle type flame bodies above and below the central lifted flame. Although these flame bodies are not seen in the prediction, they can be identified in Fig. 5 which shows the time-averaged OH distribution without applying Abel transformation for clearer observation.

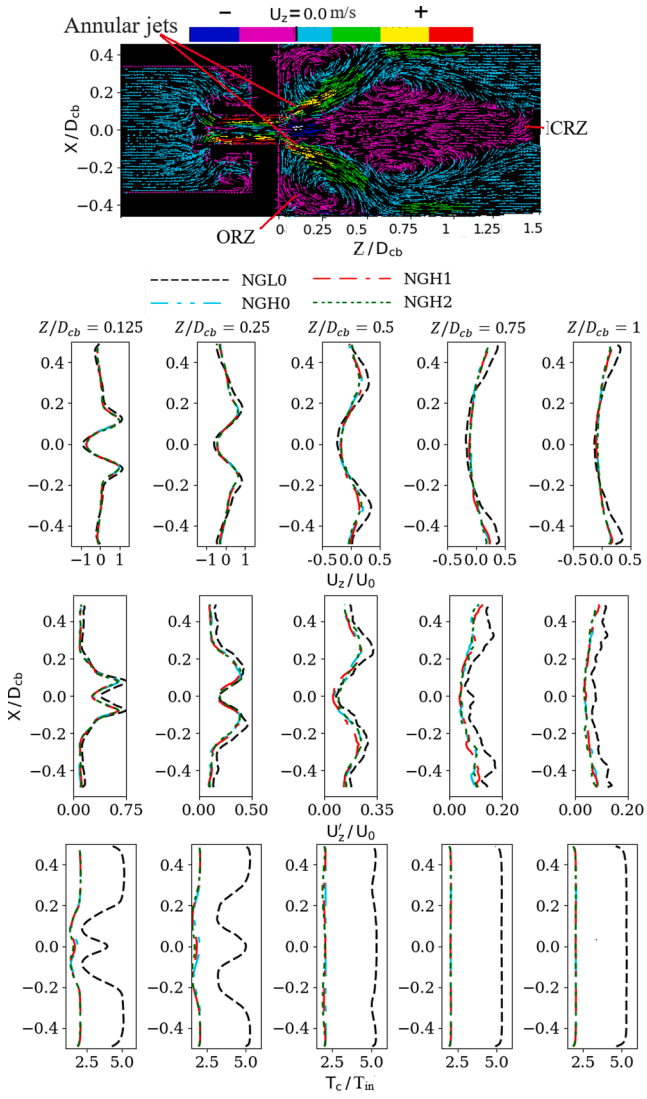

Fig. 6. Mean and RMS axial velocity, and mean temperature distributions; Representative vector plot colored by mean axial velocity.

In Fig. 5, the predicted time-averaged OH contours show that the NGH1 and NGH2 flames are of the M-type with their main flame bodies distributed along the wall. The OH can be used as an imperfect indicator of flame front location for thin flames, and it also shows the post-flame regions acting in the oxidation zone by $CO + OH = CO_2 + H$ whilst produced via the three-body reactions such as $O + H + M = OH + M$. Its formation and depletion in the high steam and low oxygen combustion environment are observed. Using CEMA enables the identification of the exact pre- and post-ignition regions of thickened flames.

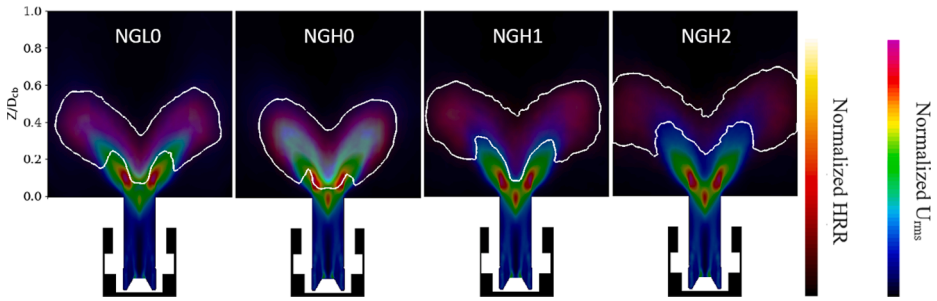

Fig. 7. RMS velocity fluctuation appended with normalized heat release rate. White contour line: normalized HRR = 10% max. HRR of the case NGH0.

In general, the OH and OH* distributions in flames are often seen to overlap partly with each other. The latter is more compact as it occurs only in the high temperature or high heat release rate zone. Since the predicted OH contour suggests that there are flames at the positions Z/D_{cb}≈0.8 and 0.2. The imperfect agreement between the predicted and experimental OH* is in line with observations by Sardeshmukh et al. [57]. It was concluded that the assumption of OH* being a quasi-steady-state (QSS) species with its transportation ignored in reaction mechanisms leads to difficulties of capturing experimental OH* distribution. This difficulty magnifies for wet flames sitting in the CDC regime as these flames are characterized by high *Ka*, *i.e.*, the chemical reaction time is much longer than the species mixing time. Besides, the imperfect agreement observed in Fig. 4 may also be caused by the thermal effect of the transparent combustor which induces noise on the line-of-sight integrated OH* measurement. Other studies [8,58] reported the experimental difficulties of capturing the exact heat release location of low O_2% CDC flames due to low OH* intensity. In 2020, Roy and Gupta [20] introduced a modified Ostu thresholding algorithm to solve the issue of unclear CDC flame images, while the method is not employed in the present work.

Overall, the main flame positions and their lift-off heights are accurately predicted and the SK30 mechanism is shown suitable for high steam-diluted combustion simulation (see Appendix B). These validate the present numerical methods to further investigate the nature of wet/CDC combustion. Also, a combustor of a smaller scale is simulated showing a good quantitative agreement between LES predictions and experimental PIV (particle imaging velocimetry) data (see Appendix A). Altogether, it gives confidence that the present simulations capture the physics and chemistry of wet turbulent combustion.

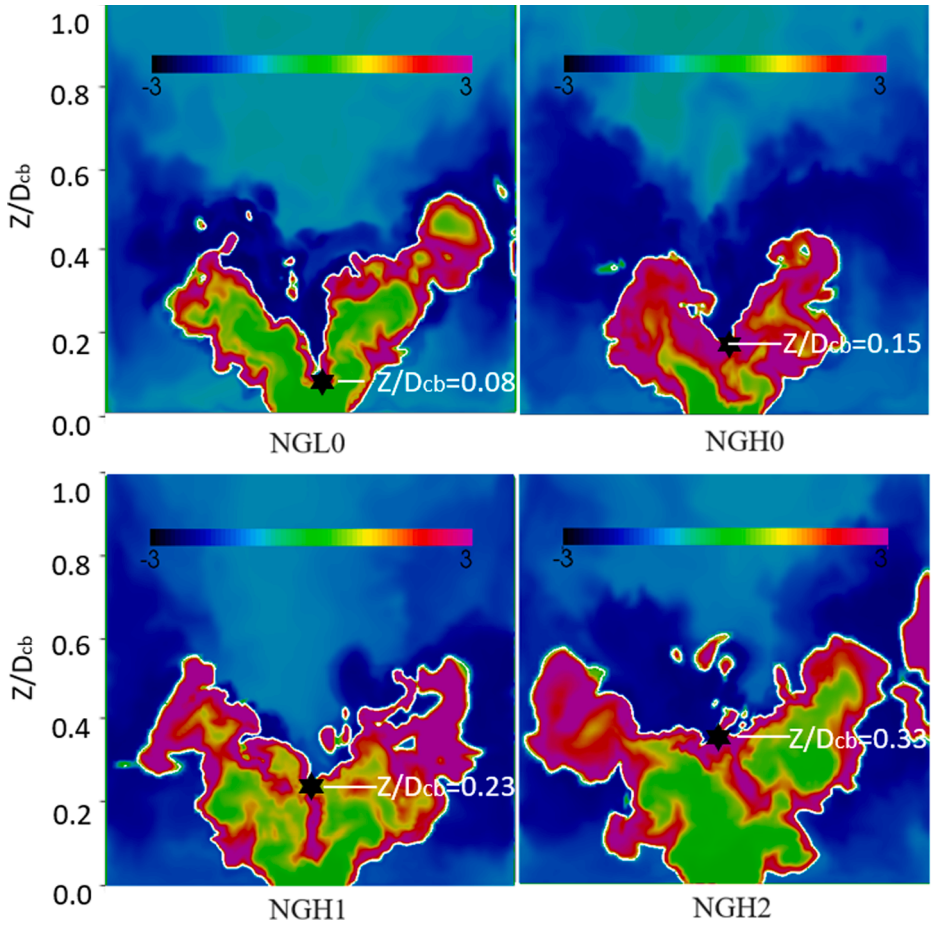

Fig. 8. Instantaneous spatial distribution of the eigenvalues of CEMs using $Re(\lambda_\omega) = sign(Re(\lambda_\omega)) \times log_{10}(1 + |Re(\lambda_\omega)|)$. The white contour line refers to the ignition boundary where $Re(\lambda_\omega) = 0$. The star symbol indicates the flame central anchoring point.

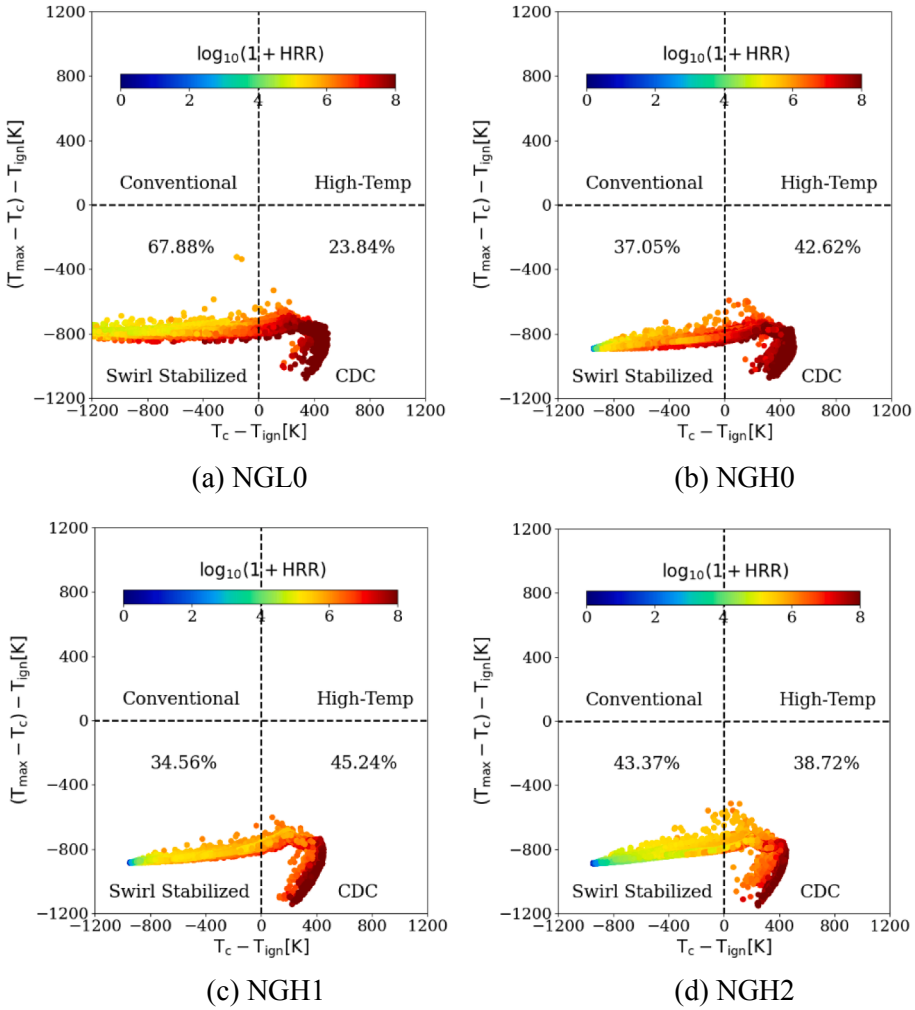

Fig. 9. Distribution of collected points ($Re(\lambda_\omega) > 0$) on the extended combustion mode graph [6]; Points colored by normalized heat release rate.

3.2. Flame and flow field characteristics

Fig. 6 presents the mean and RMS axial velocity fields normalized by the bulk velocity U_0, and the mean temperature field normalized by the inlet temperature T_{in}. The positions at which the profiles are taken can be viewed in the associated vector plot. It is seen that the axial velocity fluctuation peaks close to the exit of the mixing tube at $Z = 0.125D_{cb}$ and $X/D_{cb} \approx 0.1$, and in between the ORZs and the strongest backflow region of CRZs (blue). The peak fluctuation levels reach up to 75% of the bulk velocity. The ORZs are large extending by roughly $0.5D_{cb}$ in both radial X- and axial Z-directions, while the CRZs which are radially smaller and axially longer due to wall confinement extend from $X = 0D_{cb}$ to $0.25D_{cb}$ and $Z = 0D_{cb}$ to $1.5D_{cb}$. The recirculation zones are responsible for efficient mixing of unburnt and burnt products, driving flames towards distributed reaction zones.

For dry combustion with low $T_{in} = 293$ K (NGL0), the velocity fluctuation and the size of ORZs are seen slightly larger than the dry (NGH0) and wet (NGH1 and NGH2) combustion with high T_{in}. Note that the plots of U_z' are labeled using different X-limits, the increased difference of the axial fluctuation in the downstream than upstream is only a matter of visualization. Overall, the operating conditions have little impact on the velocity field, provided that the thermal power and T_{ad} are kept constant. In fact, the strong swirl fixes the aerodynamics – it justifies the choice of using constant T_{ad} and P_{th} to study the influence of steam dilution at nearly the same conditions of aerodynamic stabilization. The slightly higher fluctuation of axial velocity for the non-preheated case is explained by the higher thermal expansion, as reported in the literature [6–8]. The temperature distribution shows that the temperature jump across the flame is $T_{max}/T_{in} \sim 2.3$ for cases with $T_{in} = 743$ K, and $T_{max}/T_{in} \sim 5$ for the case with $T_{in} = 293$ K. The temperature ratios for all four cases simulated are lower than those of the conventional laboratory-scale flames often characterized by $T_{max}/T_{in} \sim 7$. This enables the flames investigated to move into FC or CDC regime, as will be detailly discussed in Section 3.3.

The behaviors of flames in the FC or CDC regime are presented in Fig. 7. The HRR in each image is normalized by the maximum HRR in the case NGH0. From NGH0 to NGH2, an apparent reduction of high heat release region is observed due to the increase of Ω and decrease of O_2% content. Wet flame has clearly presented a distributed reaction region and a higher lift-off height. Comparing NGL0 to NGH0, the latter shows a more compact flame with the flame base lower. Note that the ambiguous flame base and lift-off height denoted by 10%HRR are more precisely defined using CEMA in the following section. The interaction between the flame base and the RMS velocity field is of great interest that a reduced impact of velocity fluctuation on the stabilization of a lifted-like flame is expected. The details of the flow/flame interactions are being investigated by the authors via an Extended Proper Orthogonal Decomposition (EPOD) method [59].

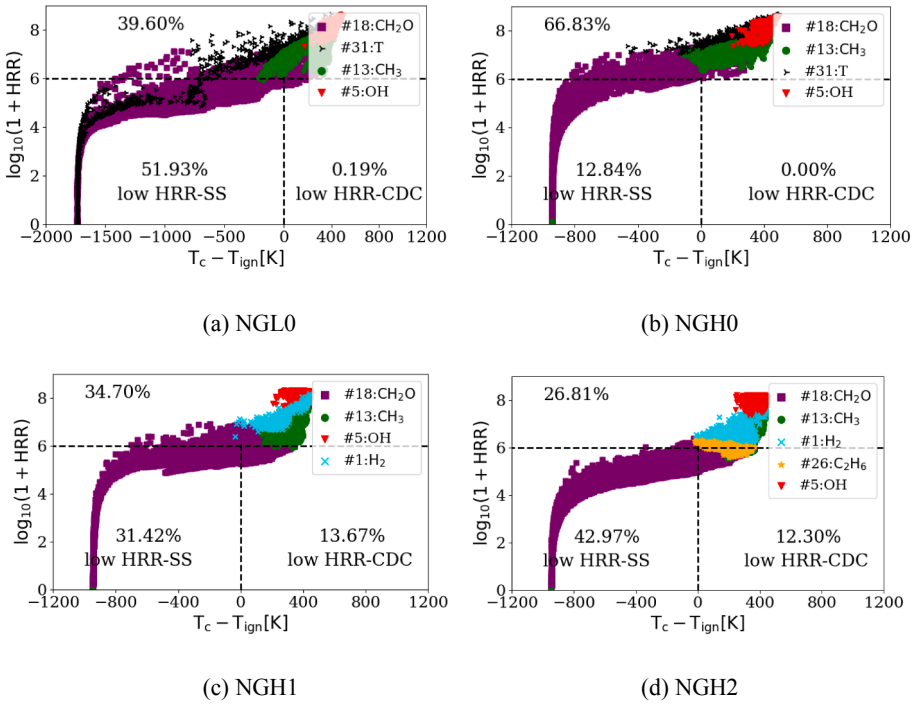

Fig. 10. Classification of collected points ($Re(\lambda_\omega) > 0$) based on normalized HRR. Point clouds colored by the dominating EI (EI_{max}) to CEMs.

3.3. CEMA analysis of flame structure

To identify the exact pre- and post-ignition regions of thickened flames characterized by the distributed reaction zone, Fig. 8 shows the eigenvalues of CEMs. The white contour lines indicate the ignition boundary where $Re(\lambda_\omega) = 0$. Within the boundary, $Re(\lambda_\omega) > 0$ implies that the unburnt mixtures are explosive. The status of these mixtures moves towards chemical equilibrium at a fast rate when isolated. Outside the boundary, mixtures are non-explosive where $Re(\lambda_\omega) < 0$ – hence burnt products are denoted by the slowest decaying mode. Compared to the non-preheated case NGL0, preheated flames show more distributed highly explosive unburnt mixtures (purple) at the vicinity of the ignition boundary indicating much thicker flame fronts. With an increase of {Ω, ϕ} and a decrease of O_2% from NGH0 to NGH2, an apparent expansion of the potentially explosive area is observed. Hence, the wet flames are characterized by explosive mixtures of fuel and products which are more distributed in the high steam-diluted, low-O_2 combustion environment. This is in contrast with that reported by Cifuentes et al. [27] due to different flow configurations employed in their work that the non-premixed flame in a Jet-in-Hot-Coflow burner is characterized by distinct ignition mechanisms, highlighting the importance of applying CEMA to premixed combustion in a high swirl burner.

Comparing Figs. 7 and 8, the advantage of applying CEMA is that the flame anchoring points can be precisely defined based on where the eigenvalues of CEMs cross zero (without arbitrarily defined threshold). Note that the anchoring points in the OH contour of Fig. 5 form a thick area separating the dark and blue colors, there is no clear indication of an ignition boundary at this location. With increasing {Ω, ϕ}, an increased lift-off height denoted by the central anchoring point is observed in Fig. 8.

3.3.1. Dilution effect on flame regime transition and EI variations

The extended combustion mode graph analysis (ECMA) proposed by Fooladgar et al. [6] is also employed to identify how {Ω, ϕ} and T_{in} affect the flame regime transition. ECMA differs from CEMA that the former calculates combustion status assuming a finite ignition time scale τ_{IG} while the latter implicitly assume a near infinitely (compared to the combustor residence time) long time for ignition. In Fig. 9, the scatter points, which are colored by log-based HRR ($log_{10}(1 + HRR)$) represent the combustion status of cells inside the CEMA identified ignition boundary. The T_{max} is the maximum cell temperature of the simulated flames, the T_c is the cell center temperature, and T_{ign} is the self-ignition temperature numerically calculated using a one-dimensional (in time) perfectly stirred reactor (PSR). The time-evolving PSRs are fed with local mixture compositions and advanced in time up to 1s [15]. Cells featuring $T_{ign} > T_{max}$ are not shown in the figure as they contain highly non-combustible mixtures. Note that though these mixtures are recognized as explosive in CEMA, they do not necessarily ignite in the PaSR configuration due to insufficient mixing with high T_c burnt product.

Fig. 9 evidences that none of the flames lie into the conventional (non-aerodynamically stabilized) or the high-temperature combustion regime since the increase of temperature $\Delta T = T_{max}–T_c$ is always lower than the ignition temperature T_{ign}. These flames cannot be self-sustained by temperature increase ($\Delta T < T_{ign}$) alone and require aerodynamic stabilization. The low T_{in} NGL0 features a lean premixed dry flame with $T_{max}/T_{in} \sim 5$ smaller than the $T_{max}/T_{in} \sim 7$ for conventional flames. Hence, it is characterized by $\Delta T < T_{ign}$ unlike that of the conventional flames.

For fluid parcels in the swirl-stabilized (SS) regime, mixtures are chemically explosive ($Re(\lambda_\omega) > 0$), while T_c (and also ΔT) is yet too low to auto-ignite the reactive mixtures. Fast mixing has brought sufficient

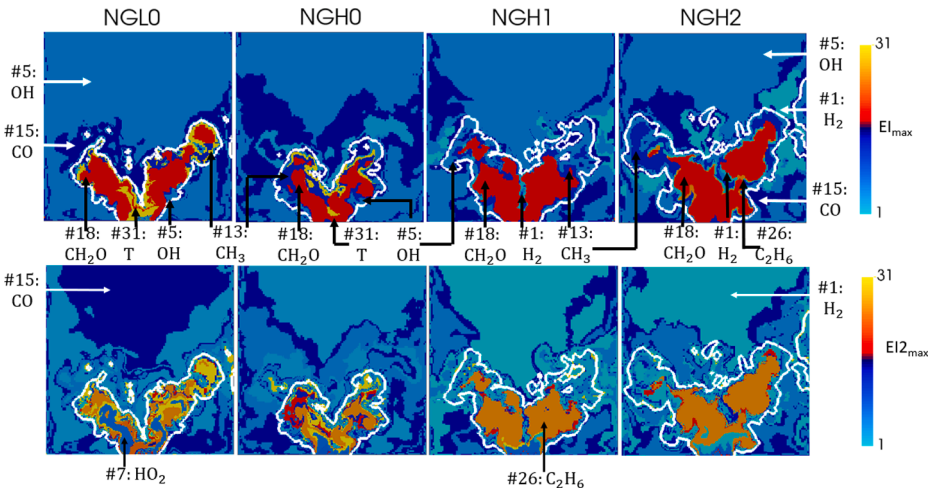

Fig. 11. Instantaneous spatial distribution of the highest (top, EI_{max}) and 2nd highest dominating EI (bottom, $EI2_{max}$). The color bar ranges from 1 to 31 associated with species variables. The white contour line refers to the ignition boundary where $Re(\lambda_\omega) = 0$.

high T_c burnt product to these cells while the local chemical reaction is too slow. This results in difficulties towards self-ignition since the increase of local T_c is lower than the increase of T_{ign}, *i.e.*,$\Delta T_c < \Delta T_{ign}$. The premixed swirling flames in the SS regime is therefore analogous to piloted/stratified flame in the pilot assisted mode [6]. The flames in the CDC regime are self-ignitable, *i.e.*, $T_c > T_{ign}$ that fast mixing brings high T_c burnt product to support combustion without over-diluting the unburnt mixtures, *i.e.*, $\Delta T_c < \Delta T_{ign}$.

Compared to dry NGH0 flame, the wet NGH1 and NGH2 flames show small variations of percentage points in different flame regimes. This is because the definition of the CDC in the extended combustion mode graph is ambiguous. The practical CDC flames often show distributed reaction zones and emit less visible radiation owing to the long reaction time and very short mixing time which dilutes reactants and avoids local sharp heat release. To develop ECMA for characterizing practical CDC flames, the regimes in Fig. 9 are split into a low and a high HRR region loosely defined using the threshold $log_{10}(1+HRR) = 6$ (approximately 20% off the maximum local heat-release), as shown in Fig. 10. The fluid parcels on the right-hand side of each image are characterized by hot, highly reactive, and hence self-ignitable mixtures. They are obtained by the rapid mixing of hot products with fresh fuel/air mixtures. The low HRR-CDC regime refers to practical CDC flames which are globally less visible characterized by low heat release rate. Fluid parcels in the low HRR-SS regime are associated with mixtures preheated by burnt products around and are characterized by low HRR, slow chemical reactions.

In Fig. 10, it is observed that,

(a) Compared to high T_{in} (NGH0) flame, low T_{in} (NGL0) combustion shows lower percentage of fluid parcels in the high HRR region. A larger region of flame in the low HRR-SS regime is hence characterized by low HRR reactions.
(b) Compared to dry (NGH0) flame, wet (NGH1 & NGH2) combustion increases not only the size of the preheating region but also the size of the self-ignitable region in the low HRR-CDC regime.
(c) Dry flames (NGL0 & NGH0) have generally followed the 1D flame structure that oxidation of methane starts from CH_2O and CH_3 ahead of the flame front then moves towards OH in the post-flame region; while wet flames show the importance of H_2 and C_2H_6 implying the activation of different oxidation pathway.

Fig. 11 shows reconstructed contour plots colored by explosion index EI from CEMA, with white lines indicating the ignition boundary. The explosion index is a normalized vector ranging from zero to unity where the EI_{max} and $EI2_{max}$ refer to the highest and 2nd highest dominating species or temperature variable to the CEMs. The importance (number of points) of EI_{max} variables follows the order of listing the species in Fig. 10.

In Figs. 10 and 11, an apparent difference between the dry (NGL0 & NGH0) and wet (NGH1 & NGH2) flames is whether temperature (variable #31) dominates the CEMs as EI_{max} variable. Lu et al. [26] classify the ignition process into two stages: the radical explosion stage dominated by radical accumulations and the thermal runaway stage dominated by temperature. At the end of an ignition process, the contribution of the latter exceeds the former. As wet flames are characterized by a much higher mixing rate than reaction rate, *i.e.*, very high local *Ka*, they do not necessarily present the end ignition process dominated by thermal runaway (for instance in the case of massive dilution by burnt products). Therefore, for wet flames, temperature domination to CEMs as EI_{max} variable or $EI2_{max}$ variable is not observed. For dry flames, the mixing rate is lower compared to wet flames, enabling the end-stage temperature contribution to CEMs as both EI_{max} and $EI2_{max}$ variables.

More specifically, in Fig. 11, dry combustion with low T_{in} (NGL0) presents temperature (variable #31) contributions to the CEM near the central flame anchoring point. The species, which represents the traditional oxidation pathway, namely: the CH_2O (species #18) dominates the explosive nature of the unburnt mixtures. It corresponds to the preheat region mostly defined in the low HRR-SS regime. Besides, a small region is affected by CH_3 (species #13) and OH (species #5) corresponding to the reacting fluid parcels in the high HRR region (refer to Fig. 10). This observation applies to dry combustion at high T_{in} (NGH0) as well, though the area dominated by temperature becomes smaller and more evenly distributed along the ignition boundary. In addition, the species CO (species #15) also contributes to the CEM in a very small region of the unburnt mixture, while it is not labeled in Fig. 11 because it is not large enough to be significant. The observations mirror the traditional structure of 1D laminar flames where CH_3 and CH_2O are species present just before the reacting zone, and OH and CO are present in the post-combustion region.

Increasing Ω to 20% (NGH1) leads to dramatic changes that the contribution of temperature to CEM is significantly lower and is hence not a strong contributor. The CH_2O (species #18) and CH_3 (species #13) are still the dominating species to CEM in the low-temperature region, followed by the promoted importance of OH (species #5) and H_2 (species #1) from outside the ignition boundary. As already discussed, the wet flame is at the radical explosion stage. The distributed reaction zone and intense mixing feature larger regions with temperature levels

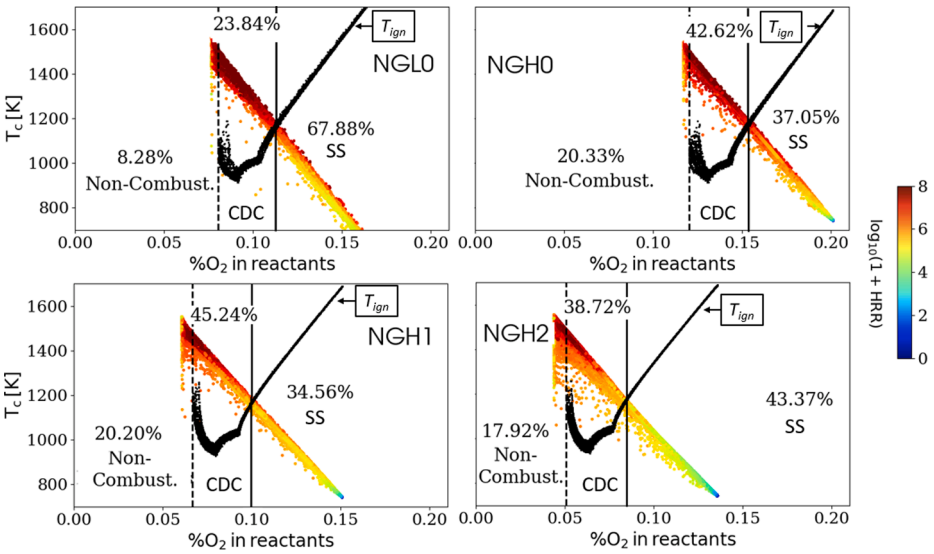

Fig. 12. Distribution of collected points ($Re(\lambda_\omega) > 0$) on the extended conventional combustion mode graph [61]; Points colored by normalized heat release rate. Black scatter points refer to self-ignition temperature. The CDC regime is separated by non-combustible points where $T_{ign} > T_{max}$ (dash line) and points in the SS regime where $T_c < T_{ign}$ (solid line).

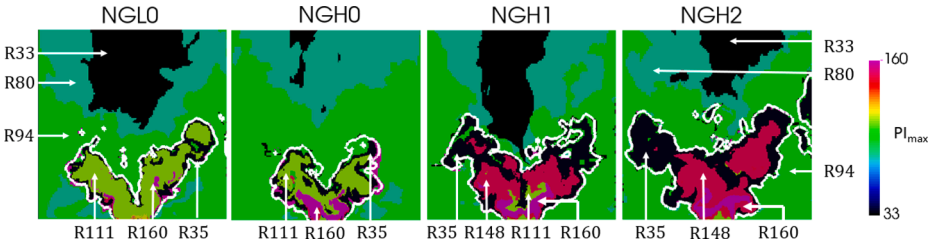

Fig. 13. Instantaneous spatial distribution of the highest dominating PI (PI_{max}). The color bar ranges from 33 to 160 associated with reaction variables. The white contour line refers to the ignition boundary where $Re(\lambda_\omega) = 0$.

between burnt and unburnt [10] – in contrast to the sharp temperature increase in thin flames. Hence, for wet flames, the temperature's participation in the CEM is less important than the reactive species. Temperature not being a dominating variable to the CEM can be used as a precursor for detecting flame transitioning into the self-ignitable, low HRR-CDC regime. The observation valid for $\Omega = 20\%$ applies as well to the case at $\Omega = 30\%$. Besides, comparing wet to dry flames, the more distributed C_2H_6 (species #26) as a 2nd dominating EI variable ($EI2_{max}$) may also be used as a precursor for flame regime transition. The role of C_2H_6 was partly reported by Tu et al. [23] that high-pressure combustion (up to 8 atm) pushes the methane/air flame from MILD to the conventional regime. Methane oxidation to form CO was classified into three routes. Route 3, which produces higher hydrocarbon molecules such as ethane via recombination was suppressed in the conventional regime and promoted in the MILD regime – an observation also thoroughly discussed by Mardani et al. [24]. A complete overview of dominating EI variables to the CEMs is provided in Appendix C, Fig. C1.

3.3.2. *Oxygen effect on flame regime transition and PI variations*

Fig. 12 shows the distribution of the explosive fluid parcels on an extended conventional combustion mode graph to explicitly show the impact of local O_2% on the regime transition. Note that the higher concentration of oxygen depends on the operation conditions. The self-ignition boundary formed by the black scatter points shows a tick mark. The lowest T_{ign} fluid parcels always lie in the CDC regime separated by non-combustible points where $T_{ign} > T_{max}$ (dash line) and points in the SS regime where $T_c < T_{ign}$ (solid line). The tick mark type of T_{ign} in Fig. 12 is different from the line shape T_{ign} reported by Medwell and Dally [60] as their conventional combustion graph was developed using global values and for lifted flames in the hot co-flow burners. Note that the black points on the left of the vertical dash line are not shown in Fig. 12 as they feature T_{ign} much higher than the range of T_c.

In Table 1, the global O_2% in reactants for the four flames are 19.7 (NGL0), 20.1 (NGH0), 15.1 (NGH1), and 13.6 (NGH2), while the self-ignitable fluid parcels in the CDC regime of Fig. 12 are filled with local O_2% in $8 \sim 11$, $12 \sim 15$, $7 \sim 10$, and $5 \sim 8$. Each flame sitting in the CDC regime allows roughly a $\sim 3\%$ change of O_2 mole fraction in reactants. Comparing the global O_2% with the mid-value of the local O_2% range, one obtains ΔO_2%=10.2, 6.6, 6.6, and 7.1 for each flame. The higher the ΔO_2%, the more mixtures are in the SS regime with combustion heavily dependent on hot product around – a combustion strategy similar to the vitiated co-flow burners (VCB) [62] – low O_2% containing mixtures require heated co-flow to sustain combustion. For instance, the NGH1 and NGH0 flames have roughly the same ΔO_2% and show almost the same percentage points in the SS. Steam in NGH1 flame ($O_2\% = 15.1$) perfectly replaces the role of oxygen ($O_2\% = 20.1$) in dry NGH0 flame via enabling low O_2% combustion.

The NGH2 flame has similarities to the NGL0 flame that they both feature higher ΔO_2% compared to NGH0 and NGH1 flames, and hence show more points in the SS regime. The difference is that the SS regime

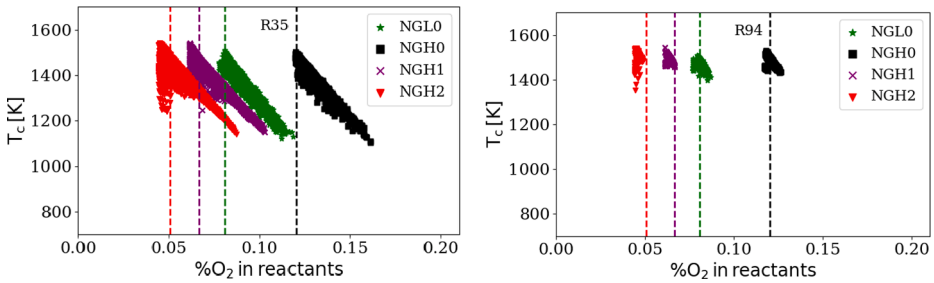

Fig. 14. Contribution of R35: $H + O_2 = O + OH$ (left) and R94: $OH + CO = H + CO_2$ (right) to flame regimes on the extended conventional combustion mode graph [61]. The dash line separates the combustible (right of the line) and non-combustible mixtures (left of the line).

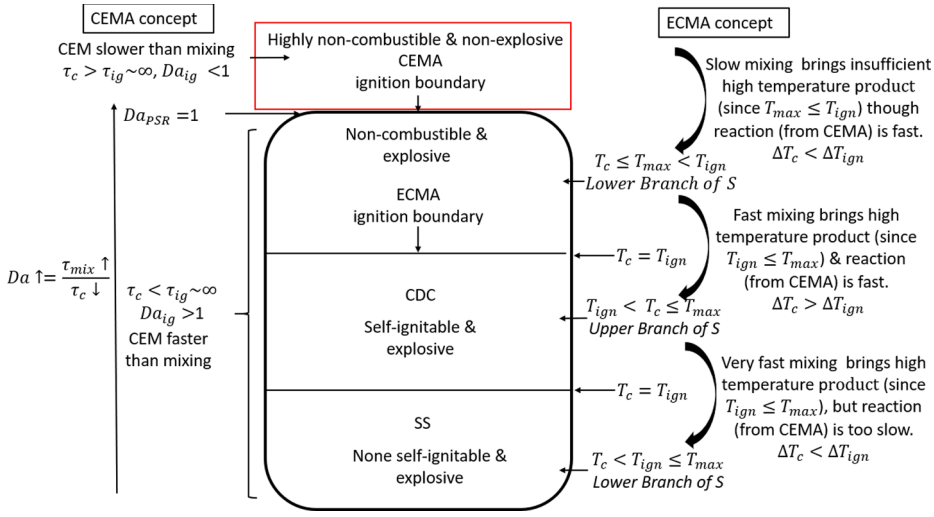

Fig 15. An overview of differences between CEMA and ECMA, and a detailed flame regime classification. $Da_{ig} = \tau_{ig}/\tau_c$.

in NGH2 is characterized by low absolute O_2% which suppresses high HRR reactions and emits less visible radiations. The NGL0 flame, due to higher O_2%, activates moderately high HRR reactions and shows attached flame behavior as opposed to the lifted flame behavior of NGH2 flame.

Fig. 13 shows reconstructed contour plots colored by participation index PI from CEMA, with white lines indicating the ignition boundary. The PI indicates how parallel a reaction is to the CEM where the PI_{max} shows the highest dominating reaction amongst all reactions. The larger the region a reaction takes, the more important the reaction is to ignite the mixtures and to sustain the entire flame. Outside the ignition boundary, mixing is much faster than the fastest chemical time scale, hence presenting no CEMs. The three important PI_{max} reactions are always R94: $OH + CO = H + CO_2$, R80: $2OH + M = H_2O_2 + M$, and R33: $H + O_2 + H_2O = HO_2 + H_2O$. The forward reaction of R94 is partly responsible to produce the intermediate H radicals which are brought into the pre-ignition region by diffusion and fast mixing. It is also responsible for consuming CO (species #15) and OH (species #5) to promote their contribution to CEMs in Fig. 11. The R33 partly consumes H radicals to promote the contribution of H_2 (species #1) outside the ignition boundary.

Inside the ignition boundary, the CEM of low T_{in} dry flame (NGL0) is mainly controlled by R111: $CH_3 + HO_2 = OH + CH_3O$, and slightly affected by R35: $H + O_2 = O + OH$ and R160: $CH_3O + O_2 = HO_2 + CH_2O$. Increasing T_{in} leads to the preheating region of the NGH flames dominated by R160. The R111 and R160 co-dominate the generation of EI_{max} variable CH_2O (species #18) in Fig. 11.

Compared to dry combustion, wet combustion (NGH1 & NGH2) results in a significant change of reactions contributing to CEMs. That is, the CH_3 radicals are not oxidized immediately by R111. Instead, the three-body ethane formation reaction R148: $2CH_3 + M = C_2H_6 + M$ dominates the CEMs, followed by the chain branching reaction R35. The reaction R148 is responsible for generating the EI_{max} variable C_2H_6 (species #26). Its forward reaction rate is promoted in the low O_2% and high steam combustion environment also reported by Mardani et al. [24]. Besides, though not indicated in Fig. 13, R94 also has a high relative influence on the CEMs inside the ignition boundary. This can be seen in Fig. 14 which summarizes the contribution of R35 and R94 to flame regimes. For each case, the dash line separates the combustible (right) and non-combustible mixtures (left).

3.3.3. *More discussions on flame regime transition/classification*

An overview of flame regime classification is provided in Fig. 15. It is worth noting that the ignition time used to define Da_{IG} should not be confused with the mixing time in $Da = \tau_{mix}/\tau_c$. For the investigated flames, Da is always smaller than unity as evidenced in Fig. 2 with local segregation factor close to unity. CEMA allows a near infinitely (compared to the combustor residence time) long time τ_{ig} for ignition. While in ECMA, T_{ign} is defined as the initial temperature at which any increments in temperature T_c move the system to the upper branch of an S-curve [11] within 1*s*. It follows the criterion used in combustion mode classification [6,15,63].

In Fig. 15, fluid parcels in the SS regime are characterized by slow and moderately fast chemical reactions as identified by CEMA. Neither heat release nor mixing is able to support self-ignition. Fluid parcels in the CDC regime are characterized by moderately fast to fast reactions,

self-ignition is achieved via either fast mixing or local high HRR. Removing high HRR fluid parcels as it is done in Fig. 10 leaves mixing as the sole contributor towards self-ignition in the practical CDC regime. Close to the CEMA boundary, non-combustible fluid parcels also feature moderately fast to fast reactions. However, slow mixing brings insufficient high temperature products leading to difficulties of self-ignition.

In Fig. 12, the non-preheating NGL0 case contains many fluid parcels defined in the SS regime. They are slowly heated by surrounding high temperature product – hence the dominating EI is temperature (variable #31). For preheated NGH flames, many parcels are defined as self-ignitable in the CDC regime – the dominating EIs are radicals. In Fig. 14, from dry (NGL0 & NGH0) to wet combustion (NGH1 & NGH2), longer chemical reaction time due to locally very lean combustion condition enables more highly non-combustible & non-explosive product such as OH and CO (from outside CEMA boundary) to join the reaction R94: $OH + CO = H + CO_2$.

Despite the limitations of CEMA in classifying premixed flame regimes and ECMA in examining the mixture's chemical reactivities/explosivity (the exact chemical time scale), analyses combining ECAM and ECMA provide new insights into the detailed flame structures of wet combustion.

4. Summary & conclusions

To guide commercial demonstration of wet combustion technology in the humidified gas turbine cycles, high fidelity large eddy simulation using finite rate chemistry was employed to study the effect of steam dilution on a swirl stabilized flame. A skeletal mechanism with 32 species and 198 reactions is used together with a partially stirred reactor closure. Four flames with different steam-to-air ratios Ω and unburnt mixture temperature T_{in} are hence studied aiming to provide insight details of flame changes when increasing the steam dilution of flame. The overall good agreements with the flame visualizations suggest the suitability of using this numerical approach to perform in-depth flame structure analyses.

Novel insights into the chemical differences between flames in the conventional and CDC regimes are explored using the CEMA method, and flame regime transitions are detected using the ECMA method. For the first time, a detailed flame regime transition graph is developed to elaborately demonstrate flame behaviors in different regimes and to distinguish CEMA and ECMA methods. Proper use of the proposed classification methods enables quantified measurement of flame behavior in the combustor of practical humidified gas turbines. For instance, adjusting combustor parameters such as mixing tube size, swirl number, *etc.* to increase percental fluid parcels in the practical CDC regime can significantly improve the performance of HGT – low emission & low instability.

From combined analyses of CEMA and ECMA, it is found that high steam-diluted, low-O_2 flames in the practical CDC regime are characterized by more distributed self-ignitable mixtures of products and fuels compared to conventional flames. Specifically, it is shown that:

- Increasing {Ω, ϕ} and decreasing O_2% promotes the lift-off heights of wet flames due to an increased number of fluid parcels in the low HRR-SS regime.
- Temperature's participation in the CEM of wet flames is less important than the reactive species, in contrast to that in dry flames.
- Temperature (variable #31) not being and C_2H_6 (species #26) being dominating EI variables to the CEM can be used as precursors to identify the flame transition from conventional to the practical CDC regime.
- Wet combustion promotes the contribution of the PI reaction R148: $2CH_3 + M = C_2H_6 + M$ to CEMs. This reaction favors the generation of the important EI variable C_2H_6 (species #26) and dominates the self-ignitable natures of wet mixtures.
- Compared to dry flame, the explosive nature of wet flames is partly dominated by the EI variable H_2 (species #1).

Besides, an extended conventional combustion mode method is proposed to show the relationship between local O_2% in reactants and flame regime transition. It is found that flame sitting in the CDC regime allows roughly a ~ 3% change of O_2 mole fraction in reactants. Wet combustion with 20% steam can perfectly replace the role of oxygen in assisting dry combustion. For wet combustion with 30% steam, however, more fluid parcels defined in the SS regime may indicate a high tendency towards local extinction compared to that of 20%.

CRediT authorship contribution statement

Kai Zhang: Methodology, Formal analysis, Investigation, Writing - original draft, Writing - review & editing. **Yazhou Shen:** Investigation, Writing - review & editing. **Christophe Duwig:** Conceptualization, Writing - review & editing, Supervision, Funding acquisition.

Declaration of Competing Interest

The authors declare that they have no known competing financial interests or personal relationships that could have appeared to influence the work reported in this paper.

Acknowledgments

The financial support from the Phoenix BioPower AB, Sweden is greatly acknowledged.

The authors would like to acknowledge the support by Simeon Dybe and Phoebe Kuhn from Hermann-Föttinger Institute Technische Universität Berlin, Germany for sharing the experimental data.

The simulations were performed on resources provided by the Swedish National Infrastructure for Computing (SNIC) at LUNARC and PDC center.

Appendix A

Grid independence study is performed by comparing LES result (mean U_z and RMS: U_z') with the isothermal ($T_{in} = 293$ K, $\dot{m}_{air}$=120Kg/h) and reacting flow measurements ($\varnothing_{CH4/air} = 0.6$), available in the literature [64]. The combustor used in that study has a small $D_{cb} = 0.105$ m, while the same swirl no. $S = 0.9$. As shown in Fig. A1, four sets of hexahedral meshes are used for comparison, each having 1 million, 2.3 million, 3.7 million and 7.85 million cells. The mesh resolution for the first two is $\Delta = 1.7$ mm and 0.83 mm. The 7.85 million mesh is obtained from the 2.3 million mesh by refining the upper half of the combustor. The 3.7 million mesh is refined only in the main flame region to reduce the computational time of reacting flow simulation. The minimum mesh resolution for the last two sets of mesh is hence the same, giving $\Delta = 0.4$ mm. The same refinement strategy is also used in the present work, see Section 2.3. <2% and 4% differences between experimental and numerical U_z & U_z' are observed in *iso*-thermal flow. The differences are roughly tripled in reacting flow while the numerical accuracy is still within an acceptable range. Lower than 2% differences amongst predictions based on the different mesh are observed, and the mesh resolution of $\Delta = 0.83$ mm is employed in the present work.

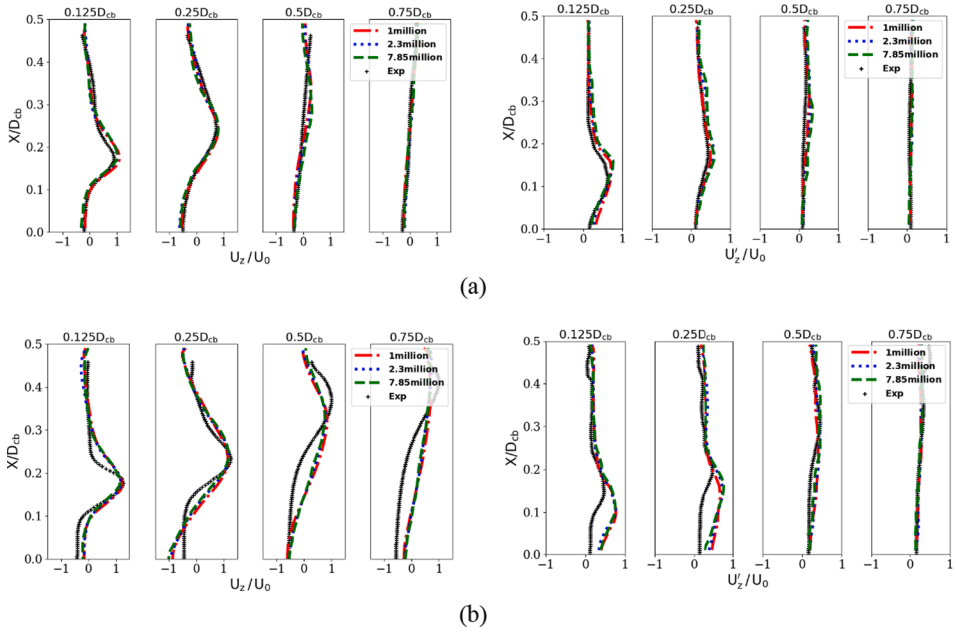

Fig. A1. Comparison between experimental [64] and numerical mean axial U_z and RMS axial velocity U_z' using different mesh size. (a) Isothermal flow; (b) Reacting flow.

Appendix B

Flame speed calculations at various equivalence ratios, different T_{in}, and steam contents are performed to validate the accuracy of the SK30 mechanism [48] in predicting steam-diluted methane combustion. In Fig. B1a ($T_{in} = 473$ K) and B.1b ($T_{in} = 373$ K), the steam mole fraction is defined as $X_{H2O} = n_{H2O}/(n_{CH4} + n_{O2} + n_{N2} + n_{H2O})$ and the equivalence ratio is defined as $\varnothing = (n_{CH4}/n_{O2})/(n_{CH4}/n_{O2})_{stoi}$. Near perfect agreement between experimental data [65] and predicted flame speed is observed even in the very oxygen and steam rich conditions when mole fraction of O_2 is up to 50% in air and$X_{H2O} = 45\%$. At $T_{in} = 300$ K, flame speed prediction using SK30 shows good agreement with experimental data reported by Boushaki et al. [66] at various equivalence ratios. Here, the equivalence ratio is defined based on the mole fraction of air, same as it is used in the present work.

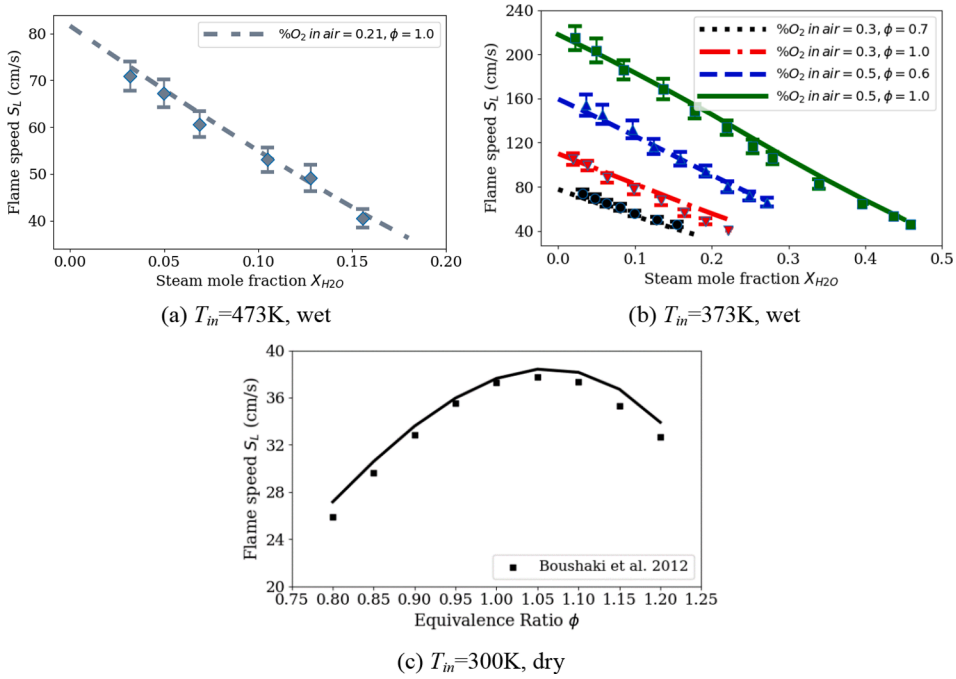

Fig. B1. Flame speed validation for steam-diluted methane combustion. (a) and (b): Mazas et al. [65]; (c) Boushaki et al. [66]; Symbols: experimental data; Lines: Prediction.

Appendix C

Fig. C1 shows the contribution of important EI variables to the CEMs of the unburnt mixture. From left to right, the increasing and decreasing importance of C_2H_6 (species #26) and T (variable #31) are interesting denoting the different stages of the methane oxidation process.

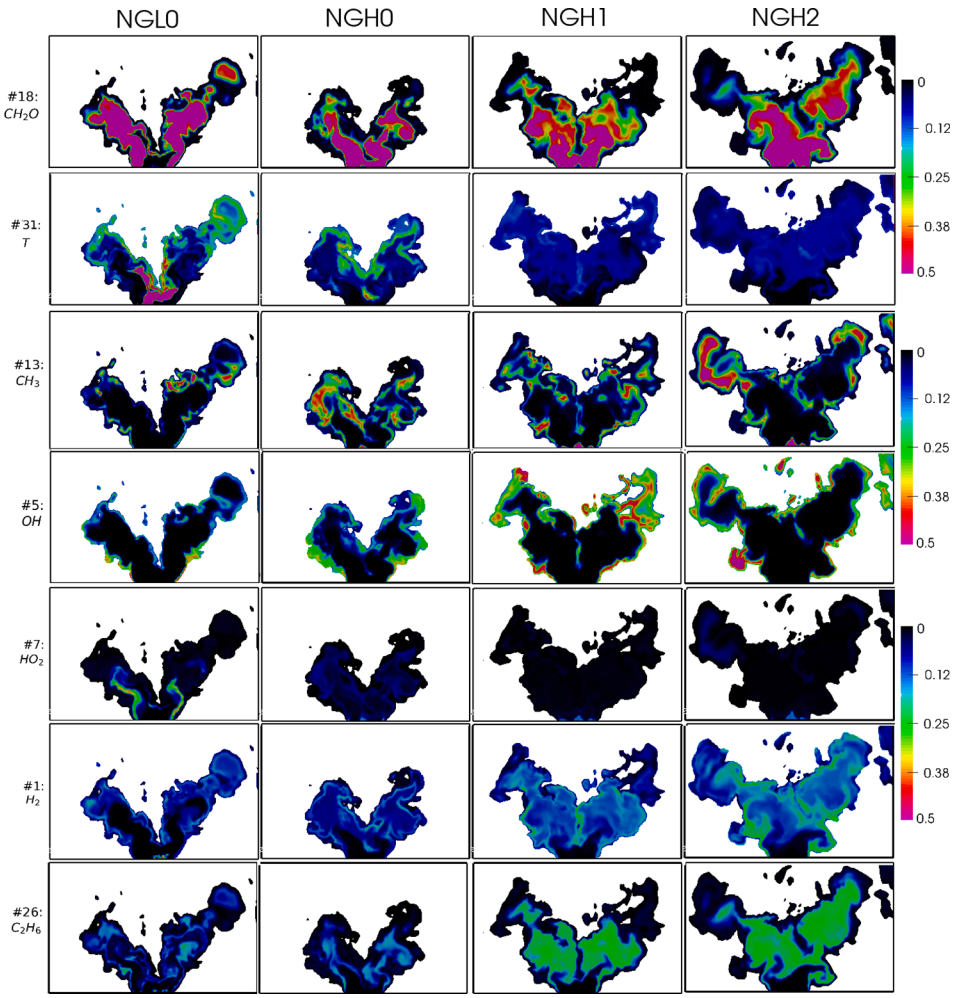

Fig. C1. Dominating explosive index variables to CEMs.

References

[1] European Commission, 2020. 2030 Climate & Energy Framework – Climate Action – European Commission. [online] Available at: <https://ec.europa.eu/clima/policies/strategies/2030_en#tab-0-0> [Accessed 22 March 2020].

[2] Bartlett MA, Westermark MO. A study of humidified gas turbines for short-term realization in midsized power generation—part I: nonintercooled cycle analysis. J. Eng. Gas Turbines Power 2005;127(1):91–9.

[3] Rydstrand MC, Westermark MO, Bartlett MA. An analysis of the efficiency and economy of humidified gas turbines in district heating applications. Energy 2004; 29(12–15):1945–61.

[4] Zhu GY, Chow TT, Fong KF, Lee CK. Comparative study on humidified gas turbine cycles with different air saturator designs. Appl Energy 2019;254:113592.

[5] De Paepe W, Carrerro MM, Bram S, Parente A, Contino F. Advanced humidified gas turbine cycle concepts applied to micro gas turbine applications for optimal waste heat recovery. Energy Procedia 2017;105:1712–8.

[6] Fooladgar E, Tóth P, Duwig C. Characterization of flameless combustion in a model gas turbine combustor using a novel post-processing tool. Combust Flame 2019; 204:356–67.

[7] Li M, Tong YH, Thern M, Klingmann J. Influence of the steam addition on premixed methane air combustion at atmospheric pressure. Energies 2017;10(7):1070.

[8] Arghode VK, Gupta AK. Effect of flow field for colorless distributed combustion (CDC) for gas turbine combustion. Appl Energy 2010;87(5):1631–40.

[9] Xing F, Kumar A, Huang Y, Chan SN, Ruan C, Gu S, et al. Flameless combustion with liquid fuel: a review focusing on fundamentals and gas turbine application. Appl Energy 2017;193:28–51.

[10] Duwig C, Stankovic D, Fuchs L, Li G, Gutmark E. Experimental and numerical study of flameless combustion in a model gas turbine combustor. Combust Sci Technol 2007;180(2):279–95.

[11] Perpignan AA, Rao AG, Roekaerts DJ. Flameless combustion and its potential towards gas turbines. Prog Energy Combust Sci 2018;69:28–62.

[12] Minamoto Y, Swaminathan N, Cant SR, Leung T. Morphological and statistical features of reaction zones in MILD and premixed combustion. Combust Flame 2014;161(11):2801–14.

[13] Zhang K, Lupo G, Duwig C. Investigation of wet combustion instability due to bio-syngas fuel variability. Fuel 2021;285:119120.

[14] Zhang K, Jiang X. Uncertainty quantification of fuel variability effects on high hydrogen content syngas combustion. Fuel 2019;257:116111.

[15] Cavaliere A, de Joannon M. Mild combustion. Prog Energy Combust Sci 2004;30 (4):329–66.

[16] Duwig C, Li B, Li ZS, Aldén M. High resolution imaging of flameless and distributed turbulent combustion. Combust Flame 2012;159(1):306–16.

[17] Khalil AE, Gupta AK. Impact of internal entrainment on high intensity distributed combustion. Appl Energy 2015;156:241–50.

[18] Khalil AE, Gupta AK. On the flame–flow interaction under distributed combustion conditions. Fuel 2016;182:17–26.

[19] Khalil AE, Gupta AK. The role of CO_2 on oxy-colorless distributed combustion. Appl Energy 2017;188:466–74.

[20] Roy R, Gupta AK. Flame structure and emission signature in distributed combustion. Fuel 2020;262:116460.

[21] Rebola A, Coelho PJ, Costa M. Assessment of the performance of several turbulence and combustion models in the numerical simulation of a flameless combustor. Combust Sci Technol 2013;185(4):600–26.

[22] Krüger O, Duwig C, Terhaar S, Paschereit CO. Large eddy simulations of methane oxidation at ultra-wet conditions in a model gas turbine combustor applying detailed chemistry. J Fluid Sci Technol 2014;9(3).
[23] Tu YJ, Xu ST, Xu MC, Liu H, Yang WM. Numerical study of methane combustion under moderate or intense low-oxygen dilution regime at elevated pressure conditions up to 8 atm. Energy 2020;197:117158.
[24] Mardani A, Tabejamaat S, Hassanpour S. Numerical study of CO and CO2 formation in CH_4/H_2 blended flame under MILD condition. Combust Flame 2013;160(9):1636–49.
[25] Wang L, Jiang Y, Qiu R. Chemical explosive mode analysis for local reignition scenarios in H2/N2 turbulent diffusion flames. Energy Fuels 2017;31(9):9939–49.
[26] Lu TF, Yoo CS, Chen JH, Law CK. Three-dimensional direct numerical simulation of a turbulent lifted hydrogen jet flame in heated coflow: a chemical explosive mode analysis. J Fluid Mech 2010;652:45–64.
[27] Cifuentes L, Fooladgar E, Duwig C. Chemical explosive mode analysis for a jet-in-hot-coflow burner operating in MILD combustion. Fuel 2018;232:712–23.
[28] Wu WT, Piao Y, Xie Q, Ren ZY. Flame diagnostics with a conservative representation of chemical explosive mode analysis. AIAA J 2019;57(4):1355–63.
[29] Wu WT, Piao Y, Liu H. Analysis of flame stabilization mechanism in a hydrogen-fueled reacting wall-jet flame. Int J Hydrogen Energy 2019;44(48):26609–23.
[30] Dybe S, Bluemner R, Zhang K, Schimet S, Duwig C, Stathopoulos P, et al. Design and experimental characterization of swirl-stabilized low calorific value gas combustion. American Society of Mechanical Engineers; 2020.
[31] Reichel TG, Terhaar S, Paschereit CO. Flashback resistance and fuel-air mixing in lean premixed hydrogen combustion. J Propul Power 2018;34(3):690–701.
[32] Vanierschot M, Müller JS, Sieber M, Percin M, van Oudheusden BW, Oberleithner K. Single-and double-helix vortex breakdown as two dominant global modes in turbulent swirling jet flow. J Fluid Mech 2020;883.
[33] Göke S, Terhaar S, Schimek S, Göckeler K, Paschereit CO. Combustion of natural gas, hydrogen and bio-fuels at ultra-wet conditions. Turbo expo: power for land, sea, and air (GT2011-45696). American Society of Mechanical Engineers; 2011.
[34] Göke S, Füri M, Bourque G, Bobusch B, Göckeler K, Krüger O, et al. Influence of steam dilution on the combustion of natural gas and hydrogen in premixed and rich-quench-lean combustors. Fuel Process Technol 2013;107:14–22.
[35] Zhang K, Dybe S, Shen Y, Schimek S, Paschereit CO, Duwig C. Experimental and numerical investigation of ultra-wet methane combustion technique for power generation. J Eng Gas Turbines Power 2020.
[36] Duwig C, Nogenmyr KJ, Chan CK, Dunn MJ. Large eddy simulations of a piloted lean premix jet flame using finite-rate chemistry. Combust Theor Model 2011;15(4):537–68.
[37] Peters N. Laminar flamelet concepts in turbulent combustion. In: Symposium (International) on combustion, Vol. 21, No. 1, p. 1231–1250. Elsevier; 1988, January.
[38] Borghi R. On the structure and morphology of turbulent premixed flames. In: Recent advances in the aerospace sciences. Boston, MA: Springer; 1985. p. 117–38.
[39] Goodwin DG, Moffat HK, Speth RL. Cantera: an object-oriented software toolkit for chemical kinetics, thermodynamics, and transport processes. Pasadena, CA: Caltech; 2009.
[40] Yu MH, Monkewitz PA. The effect of nonuniform density on the absolute instability of two-dimensional inertial jets and wakes. Phys Fluids A 1990;2(7):1175–81.
[41] Emerson B, Lieuwen T. Dynamics of harmonically excited, reacting bluff body wakes near the global hydrodynamic stability boundary. J Fluid Mech 2015;779:716–50.
[42] Duwig C, Iudiciani P. Large Eddy Simulation of turbulent combustion in a stagnation point reverse flow combustor using detailed chemistry. Fuel 2014;123:256–73.
[43] Duwig C, Dunn MJ. Large Eddy Simulation of a premixed jet flame stabilized by a vitiated co-flow: evaluation of auto-ignition tabulated chemistry. Combust Flame 2013;160(12):2879–95.
[44] Hodzic E, Alenius E, Duwig C, Szasz RS, Fuchs L. A large eddy simulation study of bluff body flame dynamics approaching blow-off. Combust Sci Technol 2017;189(7):1107–37.
[45] Zhang K, Lamorlette A. An extensive numerical study of the burning dynamics of wildland fuel using proposed configuration space. Int J Heat Mass Transf 2020;160:120174.
[46] Nicoud F, Ducros F. Subgrid-scale stress modelling based on the square of the velocity gradient tensor. Flow Turbul Combust 1999;62(3):183–200.
[47] Golovitchev VI, Chomiak J. Numerical modeling of high temperature air flameless combustion. In: Proceedings of the 4th international symposium on high temperature air combustion and gasification (HiTACG); 2001. p. 27–30.
[48] Lu T, Law CK. A criterion based on computational singular perturbation for the identification of quasi steady state species: a reduced mechanism for methane oxidation with NO chemistry. Combust Flame 2008;154(4):761–74.
[49] Kathrotia T. Reaction kinetics modeling of OH*, CH*, and C2* chemiluminescence (Doctoral dissertation).
[50] Hall JM, Petersen EL. An optimized kinetics model for OH chemiluminescence at high temperatures and atmospheric pressures. Int J Chem Kinet 2006;38(12):714–24.
[51] Lu H, Zou C, Shao S, Yao H. Large-eddy simulation of MILD combustion using partially stirred reactor approach. Proc Combust Inst 2019;37(4):4507–18.
[52] CFD Direct. Openfoam V5 User Guide: CFD Direct, Architects Of Openfoam. [online]; 2020. Available at: <https://cfd.direct/openfoam/user-guide-v5/> [Accessed 26 April 2020].
[53] Jasak H. Error analysis and estimation for the finite volume method with applications to fluid flows. Ph.D. thesis, Imperial College London, UK; 1996.
[54] Leonard BP. Simple high-accuracy resolution program for convective modelling of discontinuities. Int J Numer Meth Fluids 1988;8(10):1291–318.
[55] Lam SH, Goussis DA. The CSP method for simplifying kinetics. Int J Chem Kinet 1994;26(4):461–86.
[56] Lam SH. Using CSP to understand complex chemical kinetics. Combust Sci Technol 1993;89(5–6):375–404.
[57] Sardeshmukh S, Bedard M, Anderson W. The use of OH* and CH* as heat release markers in combustion dynamics. Int J Spray Combust Dyn 2017;9(4):409–23.
[58] Karyeyen S, Feser JS, Gupta AK. Hydrogen concentration effects on swirl-stabilized oxy-colorless distributed combustion. Fuel 2019;253:772–80.
[59] Iudiciani P, Duwig C. Large eddy simulation of the sensitivity of vortex breakdown and flame stabilisation to axial forcing. Flow Turbul Combust 2011;86(3–4):639–66.
[60] Medwell PR, Dally BB. Experimental observation of lifted flames in a heated and diluted coflow. Energy Fuels 2012;26(9):5519–27.
[61] Rao AG, Levy Y. A new combustion methodology for low emission gas turbine engines. In: 8th HiTACG conference; 2010, July. p. 13.
[62] Cabra R, Chen JY, Dibble RW, Karpetis AN, Barlow RS. Lifted methane–air jet flames in a vitiated coflow. Combust Flame 2005;143(4):491–506.
[63] Evans MJ, Medwell PR, Wu H, Stagni A, Ihme M. Classification and lift-off height prediction of non-premixed MILD and autoignitive flames. Proc Combust Inst 2017;36(3):4297–304.
[64] Kuhn P, Terhaar S, Reichel T, Paschereit CO. Design and assessment of a fuel-flexible low emission combustor for dry and steam-diluted conditions. Turbo expo: power for land, sea, and air (GT2015-43375). American Society of Mechanical Engineers; 2015.
[65] Mazas AN, Fiorina B, Lacoste DA, Schuller T. Effects of water vapor addition on the laminar burning velocity of oxygen-enriched methane flames. Combust Flame 2011;158(12):2428–40.
[66] Boushaki T, Dhué Y, Selle L, Ferret B, Poinsot T. Effects of hydrogen and steam addition on laminar burning velocity of methane–air premixed flame: experimental and numerical analysis. Int J Hydrogen Energy 2012;37(11):9412–22.